Geosci. Instrum. Method. Data Syst. Discuss., 1, 47–89, 2011
www.geosci-instrum-method-data-syst-discuss.net/1/47/2011/
doi:10.5194/gid-1-47-2011

Geoscientific Instrumentation Methods and Data Systems Discussions

Design and operation of a field telescope for cosmic ray geophysical tomography

N. Lesparre[1,*], J. Marteau[2], Y. Déclais[2], D. Gibert[1], B. Carlus[2], F. Nicollin[3], and B. Kergosien[3]

[1]Institut de Physique du Globe de Paris, UMR7154, CNRS, Sorbonne Paris Cité, Paris, France
[2]Institut de Physique Nucléaire de Lyon, UMR5822, CNRS IN2P3 – Université Lyon 1, Lyon, France
[3]Géosciences Rennes, UMR6118, CNRS – Université Rennes 1, Bât. 15 Campus de Beaulieu, 35042 Rennes cedex, France
[*]now at: Systems and Computer Engineering, Carleton University, Ottawa, Canada

Received: 18 November 2011 – Accepted: 1 December 2011 – Published: 19 December 2011

Correspondence to: N. Lesparre (lesparre@ipgp.fr)

Published by Copernicus Publications on behalf of the European Geosciences Union.

Abstract

The cosmic ray muon tomography gives an access to the density structure of geological targets. In the present article we describe a muon telescope adapted to harsh environmental conditions. In particular the design optimizes the total weight and power consumption to ease the deployment and increase the autonomy of the detector. The muon telescopes consist of at least two scintillator detection matrices readout by photosensors via optical fibres. Two photosensor options have been studied. The baseline option foresees one multianode photomultiplier (MAPM) per matrix. A second option using one multipixel photon counter (MPPC) per bar is under development. The readout electronics and data acquisition system developed for both options are detailed. We present a first data set acquired in open-sky conditions.

1 Introduction

The abundance and the large energy range of the atmospheric muons (Gaisser and Stanev, 2008), combined with the fact that the muons interact only weakly with matter, make them an appropriate probe for attempting tomographies of kilometer scale geological objects (Barrett et al., 1952). The attenuation of the flux of muons propagating through geological layers (Gaisser and Stanev, 2008) provides information on the averaged density along the muon trajectories inside the rock volume (Nagamine, 2003).

Muon radiography has first been applied in the seventies for archaeological investigations in the Egyptian Chephren pyramid (Alvarez et al., 1970). Soon later, theoretical considerations on the feasibility of muon radiography in mining engineering appeared in the geophysical literature (Malmqvist et al., 1979). The idea of muon radiography in volcanic studies first appeared in 1995 (Nagamine, 1995; Nagamine et al., 1995) and further development in a detector design and a data analysis method has been worked out (Tanaka et al., 2003). The first muon radiography of a volcano was obtained by

Tanaka et al. (2005). These pioneering studies, soon followed by further experiments, aimed at detecting both spatial and temporal variations of density inside volcanoes (Tanaka et al., 2009, 2010 and reference therein).

We develop cosmic ray telescopes designed for imaging geological targets with a thickness of rock between 50 and 1500 m. The detection time from each measurement location has to remain less than six months, to construct in a few years a tomography of the object. This method allows the detection of objects with a spatial resolution between 10 and 40 m, for telescopes with an angular resolution of about 0.1 rad. The density variations detectable with such a method could be as low as 3 %, depending on the rock opacity as well as on the respective sizes of the target and the heterogeneities (Lesparre et al., 2010). Some first acquisitions have to be realised in open sky conditions to control the telescopes' bars efficiency and calibrate their set-up (Lesparre et al., 2011).

The attenuation, from which the opacity is deduced, is determined by comparing the muon flux, I, measured after crossing the geological target to the incident flux, I_0, measured in open sky conditions at a same altitude and for the same zenith angles. These muon flux, expressed in $\text{cm}^{-2}\,\text{sr}^{-1}\,\text{s}^{-1}$, correspond to the integration of the muon energy spectra Φ between the minimum energy to reach the sensor E_{min} and the infinite. Obviously, a very precise estimate of Φ is of a critical importance since it directly influences the measurement of the attenuation in the geological body. Some Φ models proposed by different authors are used, but due to their yet strong uncertainty, the experimental flux measured in open sky condition for each experiment should also be used to derive the attenuation (Lesparre et al., 2010).

The feasibility of muon radiography is now well established and the present challenge is to perform full 3-D tomography by placing muon telescopes all around the geological target to obtain the multi-directional ray coverage necessary to solve the inverse problem of 3-D tomography (Mohamma-Djafari and Dinten, 2008). A first study of this kind was recently performed by Tanaka et al. (2010). This objective poses a number of practical problems because many geological targets of interest are explosive volcanoes with unstable steep topography, located in remote tropical areas with harsh environmental conditions (Gibert et al., 2010; Marteau et al., 2011).

In the present paper, we describe cosmic ray telescopes designed for such field environment. These telescopes are intended to operate on tropical volcanoes like La Soufrière of Guadeloupe with a relative humidity higher than 95 %, heavy rains and strong winds. There, most telescope locations are far from roads and power lines, and the total weight and power consumption must be low enough to allow both helicopter hauling and solar panel powering. In this paper we present the detection system and the data acquisition chain in Sects. 2 and 3, the mechanical frame and the field conditioning equipments (wireless links, solar panels) in Sect. 4 and the telescope response calibration for open sky conditions in Sect. 5. Finally, we end with first field measurements.

2 Detection system

2.1 Scintillator bars, wavelength shifting optical fibres and optical plugs

Different detection techniques are available: emulsions (Tanaka et al., 2007), resistive plate chambers (De Asmundis et al., 2007), micromegas (Giomataris et al., 2006), scintillators (Pla-Dalmau et al., 2001). We retained the scintillator bars option to build the detection matrices since plastic scintillators are known to be robust, light, low-cost detectors particularly well suited to field conditions and actually used for most studies on volcanoes (Tanaka et al., 2005; Gibert et al., 2010). Furthermore, scintillators allow the use of the compact OPERA data acquisition system described later in the present paper.

The scintillator bars were provided by the Fermi national accelerator laboratory. They have a rectangular cross-section of $5 \times 1\,\mathrm{cm}^2$ and are co-extruded with a TiO_2 reflective coating and a 1.5 mm diameter central duct to host an optical fibre for light collection (Pla-Dalmau et al., 2001). The scintillator is made of polystyrene mixed with a dopant

GID
1, 47–89, 2011

(1 % PPO and 0.03 % POPOP) increasing the signal produced by the ionizing particles and a fluorescent compound emitting in the blue waveband (OPERA collaboration, 1999). The transmittance spectrum of the scintillator strips shows an absorption cut-off at about 400 nm and an emission peak at 420 nm (Pla-Dalmau et al., 2001, 2003). The ruggedness of the coating allows a direct application of glue on the strips to assemble them (MINERvA collaboration, 2006). The extremities of the strips are free of coating and covered with a white reflective paint (Bicron BC-620) to increase the light yield (Pla-Dalmau et al., 2005).

The photons produced in a scintillator bar are collected by a wavelength shifting (WLS) optical fibre (Bicron BCF 91A MC) glued with an optical cement (Bicron BC-600) in the central duct of the bar. The fibre has absorption and emission peaks at 430 and 495 nm respectively due to the action of the fluorescent dopant contained in the core. The optical cement has a refractive index of 1.56, the core (polystyrene) and the clad (acrylic) of the WLS fibre have a refractive index of 1.6 and 1.4, respectively.

The WLS fibres are only polished at one end since their length (0.8, 1.2 or 1.6 m) is short compared to the light attenuation length (approximatively 10 m). This extremity of the fibre is glued in an optical plug itself glued in the scintillator bar. A plug counts three elements (Fig. 1) machined in PEEK (PolyEtherEtherKetone) material and designed to receive either a clear optic fibre (Bicron BCF-98 MC) or a Multi-Pixel Photon Counter (see Sect. 2.3).

2.2 Matrices of scintillator bars

The scintillator bars described above are aligned in the orthogonal X and Y directions to form a checker-board arrangement constituting a matrix whose $5\times5\,\mathrm{cm}^2$ pixels are defined as the intersections of the X and Y bars (Fig. 2). We built such matrices with 16×16 and 24×32 pixels, respectively. The smaller matrices with a size of $0.8\times0.8 = 0.64\,\mathrm{m}^2$ were the first built to validate the manufacturing procedure. The larger matrices offer a larger detection area which reduces the acquisition time for a given angular resolution (Lesparre et al., 2010).

GID
1, 47–89, 2011
A field telescope for cosmic ray geophysical tomography
N. Lesparre et al.

The two X and Y scintillator layers are encapsulated by 1.5 mm thick anodised aluminium plates. The four edges of the matrix are filled with a black polyurethane resin (Axson RE-11820-95) to form a compact self-supporting rigid board protected against light and humidity (Fig. 2). The three aluminium sheets are grounded with a common copper adhesive tape to avoid capacitor phenomena. The total thickness of a matrix is of about 26 mm for a weight of 25 kg for a 16×16 matrix. One telescope contains at least two matrices (Fig. 3) to define the trajectory of a detected particle from the pixels fired on each matrix. The total aperture angle and the angular resolution of the telescope may be adjusted by changing the distance between the matrices. For instance, for distances of 90, 115 and 150 cm, the total aperture angular are of 1.5, 1.2 and 1.0 rad for angular resolutions of 111, 87 and 66 mrad, respectively.

2.3 Photomultipliers and cookie

Two types of photomultipliers may be adapted to the matrices. The first type is a 64-channels Multi-Anode PhotoMultiplier (MAPM) connected to the matrix bars through clear optical fibres, and the second type is for Multi-Pixel Photon Counter (MPPC or Silicon PM, SiPM) directly connected onto the optical plugs of the scintillator bars.

MAPM requires clear optical fibres connection to guide the light from the scintillator bars to the sensor's entrance window. Depending on the size of the matrix, up to 64 fibres may be glued in a dedicated cookie which insures the fibre-to-pixel alignment (Fig. 1 bottom). The clear fibres are covered with a black coat to insure light tightness. The cookie is machined in black PEEK and contains a light diffusing system with a LED to calibrate in-situ the MAPM response. Although the use of optical grease (Nuclear Enterprise NE588) increases the coupling by up to 20 %, the large time-variations and larger gain non-uniformity which have been observed lead us to prefer a direct contact between the MAPM external window and the cookie.

Our first telescopes are readout with MAPMs (Hamamatsu H8804-mod1) compatible with the data acquisition system already developed for the OPERA Target Tracker experiment (Adam et al., 2007). The MAPM has a time resolution between 2 and

GID
1, 47–89, 2011

5 ns and a spectral response ranging from 300 and 650 nm, Table 1. The MAPM survival rate is of 100 %, their gain and pedestal variations measured on field are lower than 10 % and 1 %, respectively (Fig. 4). Two upgraded versions of this MAPM have been tested and/or used: H8804-mod5 (similar to H8804-mod1 but for the pinout) and H8804-200mod5 with a so-called extended photocathode leading to an increase of quantum efficiency up to 30 % (Fig. 5).

The MPPCs (Hamamatsu S10362-11 series ref. 050C and 100C) have very attractive performances in terms of low light level detection, single photon sensitivity and photon number resolution power. Their form factor and ceramic packaging are optimal for the coupling to scintillator (Fig. 6). They fit into the optical plugs originally designed for the clear fibres used in the MAPM option (Fig. 1). Their main features are summarized in Table 1.

The use of MPPC allows to improve the signal to noise ratio and therefore the muon detection efficiency. The matrix design is also simplified since clear fibres are no more necessary. This is clear advantage during all transportation phases where vibrations may damage the fibres or weaken the optical connections. Moreover, no cross-talk is generated at the photomultiplier level. The dark count rate and the thermal fluctuations of the MPPC performances are the most critical features for this type of sensor. While the dark count rate may be controlled by setting a large enough threshold, the thermal fluctuations may be more difficult to reduce in outdoor environments. As an example the dark count rate may double every 9 °C approximately and high temperature/humidity may affect the device lifetime.

So the main modification to the sensor which has to be performed is the integration of Peltier cells to ensure the temperature stability inside the enclosure containing the MPPCs and a feedback loop in the electronics to finely adjust the bias voltage according to the changes in temperature. The MPPC option is currently under final validation, see for instance the developments in the electronics readout in the next Section. A MPPC matrix is currently used for tests in our laboratories and we foresee to include progressively MPPC matrices in our telescopes, first with MAPM matrices (hybrid option)

GID
1, 47–89, 2011

Title Page
Abstract | Introduction
Conclusions | References
Tables | Figures
◀| |▶
◀ ▶
Back | Close
Full Screen / Esc
Printer-friendly Version
Interactive Discussion

to compare the performances between the two readout options and then as unique detection device.

3 Readout system

The global data acquisition system is built as a network of “smart sensors”. The MAPM data are collected by two multichannel front-end chips, then digitized and pre-processed by an Ethernet Controller Module (ECM) plugged on a Controller Mother Board (CMB) (Fig. 7). The same type of architecture is also valid for the MPPC option where only the front-end stage has to be adapted. The data acquisition system performs the detector configuration, the monitoring, the event building and data transfer to the on-board computer. The distributed client/server software is based on the Common Object Request Broker Architecture (CORBA) standard which is a well-known object-oriented application (www.corba.org). Since the telescope is running in triggerless mode, event timestamp accuracy is a critical issue. A clock broadcasting system synchronizes all sensors with a common clock unit regulated by GPS.

3.1 Front-end board

Each photomultiplier is read out by two multichannel front-end chips, one for each direction X and Y. They were designed in the AMS BiCMOS 0.8 µm technology at the Linear Accelerator Laboratory (LAL IN2P3 Orsay, France) for the OPERA experiment (Lucotte et al., 2004) (Fig. 8). Each channel of the chip contains a low-noise variable-gain preamplifier which uses switchable current mirrors with various areas to reach effective gain correction factors ranging from 0 to 3.9. The amplified current enters a standard 2-arms architecture: a *fast shaper arm* for the trigger and a *slow shaper arm* for a precise charge measurement.

The fast shaper has a typical gain of 2.5 $\mathrm{VpC^{-1}}$, a peaking time around 10 ns, and it is followed by a comparator with a threshold set externally. When the threshold is exceeded on at least one channel, the trigger initiates the charge read out in the slow shaper arm. The trigger efficiency is 100 % at 1/10th of photo-electron. Due to the harsher conditions with respect to power supplies and ground connections on field, we operate the telescope with a threshold equivalent to 1 photo-electron while the calibration tests in the laboratory were performed with lower thresholds (typically 0.3 photo-electron).

The slow shaper has a gain of 120 mV pC^{-1}, a peaking time of 160 ns, and the linearity of the charge measurement is better than 2 % over the full dynamic range (1–100 photo-electrons). The charges are stored in 2 pF capacitors and the channels are sequentially readout at a frequency of 5 MHz. A total time of 12.8 µs is required to readout a MAPM after reception of a trigger, setting the dead-time scale of each telescope plane. The chip consumption is about 150 mW pC^{-1} for 32 channels and the electronic cross-talk has been measured to be negligible with respect to optical cross-talk which is around 2 %.

The two multichannel front-end chips are located on a single front-end board which also receives the MAPM plugged on a 8×8 matrix. Four independent pins are for high voltage and ground connection. The connections to the CMB are made through two 26-pins flat cables for both the analogue and digital I/O and a shielded cable is used for the high voltage.

3.2 Ethernet controller mezzanine and controller mother board

The core of the data acquisition system is the ECM, connected to the CMB (Girerd et al., 2000; Marteau, 2009). It includes a sequencer (FPGA from the Cyclone ALTERA family), an external FIFO and a microprocessor (ETRAX 100lx from AXIS, www.axis.com) with an Ethernet interface. The FPGA performs the sequencing of the readout (clocks, R/O registers, digital I/O), the local data pre-processing (zero suppression, external trigger on request), the event time stamping via a local fine counter cycling at 100 MHz and synchronized with the global distributed clock, and the data transfer to the external FIFO. The microprocessor accesses the data from this FIFO for

GID
1, 47–89, 2011

further processing, formatting and data transfer. It is a 32-bit RISC CPU with a Linux 2.4 operating system mounted in a multi-chip module with: an Ethernet transceiver (supporting rates up to 200 Mbits s^{-1}), a 4 Mbytes flash memory card, and a 16 Mbytes SDRAM. The trigger architecture is described below. Each retained event contains the signal intensity (in ADC counts), the timestamp (10 ns accuracy) and the X and Y coordinates of the interaction. The readout is running continuously, data are processed and filtered online and stored locally.

The module (ISEG BPn-10-165-12K, http://www.iseg-hv.com) providing the high voltage required by the MAPM is also located on the CMB to avoid an external high voltage line. The output voltage is adjustable from 0 to −100 V via an external control voltage with a range of 0–5 V and an accuracy of ±1 %. The mean time between failure of the module exceeds 300 000 h at full load and for a temperature of 25 °C. The ripple is less than 0.01 % peak-to-peak.

3.3 Dedicated electronics for MPPCs

In order to use the same kind of sensor network for telescopes using MAPM or MPPCs, we developed a dedicated electronics board using the same staged structure (Fig. 9). The front-end stage uses the SPIROC, a MPPC Integrated ReadOut Chip, developed at LAL (Bouchel et al., 2009). The first version foresees only the use of the preamplifier, trigger and shaper stages of the chip. The connector visible on the left side of Fig. 9 is for the connections with the MPPCs. A common bias voltage is distributed through a serial connector. The SPIROC chip and the ECM are placed in the middle of the board. The MPPC readout system is fully compatible with the MAPM option, both sensors being seen as nodes of the Ethernet network. The readout sequences are obviously the same as well as the data format. This development strategy will allow a detailed cross-check of both options when the MPPC system will be mature enough to be integrated on a field telescope.

3.4 Clock distribution system

A global common clock is necessary to synchronize all nodes of the distributed system. The bi-directionality of the system allows the control of the signal reception and the measurement of the propagation time with acknowledgement signals (Marteau, 2009). The clock distribution system starts from the GPS control unit which sends a 20 MHz clock with encoded commands to the distributed sensors through a multipoint low-voltage differential signaling bus. This signal is generated with a precise and stable oscillator and is received/decoded by the clock system unit of each ECM. Each ECM uses a local 100 MHz oscillator which is locked via a standard phase locked loop to the precise clock. These local counters are reset each cycle (1 cycle = 1 s) by a specific signal to avoid relative shifts in time between all sensors connected. After correction of the propagation delays the value of the local fine counters on each sensors is used for the event time stamping, ensuring an overall accuracy of 10 ns well adapted for defining coincident events between the detection planes during the event building phase. The coincidence window for XY coincidence is of 10 ns at maximum, since it represents one clock shot.

3.5 On-board computer

The on-board computer is linked via the Ethernet switch to the ECMs and to the WiFi antenna through which it communicates with the outside and acts as a gateway for the whole system. The choice of the hardware was motivated by different considerations and constraints induced by the experiment: its size, field of operation and need of autonomy. The computer has been assembled by eviGroup (http://www.evi-group.fr) with off-the-shelf components so as to answer to our needs: simplicity and stability, low consumption, use of market standards. Its relevant characteristics are summarized in Table 2. The CPU can be down-clocked to 1 GHz to further reduce power consumption. The operating system is Linux Xubuntu 10.04 “Lucid Lynx” (http://www.xubuntu.org).

GID
1, 47–89, 2011

3.6 Trigger and readout scheme

The data acquisition (DAQ) system of each matrix is fully distributed over the local Ethernet network. It involves two major processes: a sensor application (one per sensor) and a DAQ application (one per telescope) for data collection and event building. The entire communication scheme between those processes is based upon CORBA architecture, which is a standard for distributed method invocation over a network, in its omniORB implementation (http://omniorb.sourceforge.net).

The trigger scheme is based on a dual level architecture: L0 (level 0) applied on the individual plane sensors and L1 (level 1) applied online by the DAQ mini-PC to the telescope data collected from all planes. The triggering conditions during a standard run are the following:

- L0: at least 1 channel above 1 photo-electron threshold and at least 1 channel above zero suppression threshold (0.2 photo-electron) in the opposite direction (i.e. 1 XY coincidence required in a time of 10 ns)

- L1: majority condition: at least 2 L0 triggers in time coincidence within a typical 100 ns gate.

All the triggering parameters stated above are adjustable online by software.

The on-board computer acts as the server: it runs the DAQ software that periodically interrogates on a per-cycle basis the sensor applications to retrieve the list of hits: these lists are merged and sorted in time, then, an algorithm is applied, looking for time coincidences and possible clustering logic. Specific cuts on hit position, energy, multiplicity may be applied afterwards. Data are then written directly on hard disk. SQLite, a light data base system is used to handle locally all the configuration and calibration parameters of the whole acquisition system (www.sqlite.org). The DAQ application offers as well a graphical user interface to handle the data acquisition telescope. It offers a full access to all sensors for activation/deactivation, calibration and configuration, and at the telescope level, it allows run start/stop and calibration start/stop.

GID
1, 47–89, 2011

4 Field telescope

4.1 Mechanical structure

The components described in the preceding Sections were assembled into a robust telescope that can be installed in a harsh environment. Generally a telescope includes two matrices as shown Fig. 3, but a three-matrices arrangement may be useful to better suppress fake tracks made by two charged particles interacting simultaneously with the two matrices of detection (Nagamine, 2003). In some other case, thick iron plates with a thickness of at least 2 cm may be necessary to filter electrons (Nagamine, 2003).

The telescope structure must be adaptable to host these optional equipments and to adjust the distance between the matrices in order to adapt the total angular aperture. Moreover the frame must be modular to facilitate both the transportation and the installation on the field. Accounting for these constrains, the frame of the telescope is built with slotted and anodised aluminium profiles.

A scintillator matrix and its devices (cookie, MAPM, front-end, ECM and power supply) are placed in a single box made with 4 profiles and two 1 mm thick aluminium plates (Fig. 10 left). The interior of the box is painted in black to dump the effects of potential light leaks and the matrix is secured by means of two bars of profile. The total mass of the box amounts to 45 kg for a 16×16 pixels matrix and handles are distributed along the frame for easier manipulation. Water and light tightness is obtained with a seal applied between the aluminium plates and the profiles. Four connectors complying with the IP67 norm are used to ensure power supply and data transfer and a valve equipped with a Gore Tex membrane allows evacuation of water vapour without letting liquid water to penetrate into the box. This simple device proved very efficient to reduce the relative humidity in the box, for instance, on la Soufrière, the relative humidity varies around 70 % in the box while it is higher than 95 % outside. We checked that the environmental conditions in the box were always above the dew point.

The supporting structure of the telescope is made with the same aluminium profile used for the matrix boxes (Fig. 10 middle) and it is composed of two rectangular rigid

GID
1, 47–89, 2011

A field telescope for cosmic ray geophysical tomography

N. Lesparre et al.

frames and of optional bars to support the tarpaulin (Fig. 10 right). The rectangular frames are articulated to fix the inclination of the matrices, and the lower frame can be either equipped with wheels or with adjustable legs suitable for rough topography. Auxiliary anchors may be placed elsewhere on the frames to fix stabilizing cables.

The common electronic devices (on-board computer, data logger, DC-DC converters, Ethernet switch, clock board) are placed in an aluminium case also equipped with a Gore Tex membrane. This box is hermetically closed against water and dust, and its metallic surface is sufficiently large to ensure good thermal dissipation. In practice, the temperature rarely reaches 45 °C.

Excepted for the boxes containing the scintillator matrices, the whole telescope may be disassembled in elements of less than 20 kg.

4.2 Environmental sensors

Several temperature and relative humidity sensors are placed in the matrix and electronic boxes as well as on the telescope frame to monitor the environmental parameters outside and in the different cases, providing the ambient conditions of the electronics. Two inclinometers are placed on the frame to monitor the orientation of the telescope and check that no catastrophic overturn occurred. The voltage of the power supply is also measured to check the efficiency of the accumulator charged by the solar panels.

All data are collected by a data logger (e.Reader from Gantner, www.bgp.fr) which daily sends its data files to the on-board computer through a ftp connexion. In order to reduce its power consumption to 100 mW, the data logger is almost always in sleeping mode and wakes up every 15 min to perform data logging.

4.3 Electrical power and WiFi link

The overall power consumption of the telescope is of about 35 W (Table 3) and allows the use of solar units to provide electrical energy. Eventually, in an environment where volcanic ash may alter the solar panels, combustible cells may be used as well. The

GID
1, 47–89, 2011

total power of solar units to be installed depends on the meteorological conditions encountered on field. For instance, the cloudy weather generally present on La Soufrière of Guadeloupe implies to apply a security factor of at least 15 to prevent from power failure during long cloudy periods where the solar panels are not efficient enough to refill the accumulators. For this reason, on this volcano, we use two solar units with a maximum power capacity of about 540 W (Fig. 10 right).

WiFi antennas are used to establish a permanent link with the telescope in order to both transfer data and perform a real time monitoring. We use long-range antennas enabling wireless transmission over distance of 40 km (Ubiquiti PS5, www.ubnt.com).

5 Calibration of the telescope response

5.1 Photomultiplier calibration

A first calibration concerns the equalization of the MAPM channels in order to work with a single threshold for all channels and therefore simplify the trigger logic. A blue-light LED diffusing system is plugged on the cookie (Fig. 1) to calibrate the MAPM response by a statistical analysis of each MAPM channel spectra, fitted with a Bellamy model (Bellamy et al., 1994) which leads to an average 10 % accuracy on the parameters value (Fig. 11). The LED system is used both for calibrating each MAPMT, as described in the following, and for monitoring the system stability in situ.

The MAPM response to a light pulse results from both the detection of the emitted photons and the signal amplification. A background thermal noise present even in the darkness disturbs this signal. For high-intensity light pulses, the response, $\mathcal{R}_{\text{MAPM}}$, of a MAPM channel is approximated by,

GID
1, 47–89, 2011

$$\mathcal{R}_{\mathrm{MAPM}}(x) = \frac{1}{\sqrt{2\pi\mu(\sigma_1^2+g_1^2)}} \times \exp\left(-\frac{(x-g_0-w/\alpha-\mu g_1)^2}{2\mu(\sigma_1^2+g_1^2)}\right), \quad (1)$$

where g_1 is the average charge at the photomultiplier output when one photo-electron is collected and σ_1 is the standard deviation of the charge distribution. The mean number of photo-electrons collected, μ, is proportional to the light source intensity. g_0 is the pedestal average charge with standard deviation σ_0. w is the probability of a discrete background noise component with an exponential decrease coefficient α (Bellamy et al., 1994).

The calibration procedure of a MAPM proceeds as follows:

1. LED spectra fitting at HV = –850 V with 1–2 photo-electrons injected on average,
2. identification of the channel(s) with the maximal response (gain),
3. first raw correction of the high voltage to fix the maximal response at 10^6 using a scaling law such as the gain is set proportional to a power law of HV,
4. first determination of $\mathcal{R}_{\mathrm{MAPM}}$ parameters Eq. (1),
5. equalization of the 64 channels gains and insertion of the shift register parameters in the front-end electronics,
6. LED spectra fitting in this new configuration,
7. second iteration of the procedure if necessary,
8. threshold setting around 0.1 photo-electron, measurement of the dark count rate in auto-triggering mode.

GID
1, 47–89, 2011

The gain distributions of the 64 MAPM channels before and after the gain equalisation are shown in Fig. 12.

Finally the MAPM is connected to the telescope plane and the counting rate is measured in auto-triggering mode. As the counting rate includes the natural radioactivity and the MAPM dark current of the isolated channels as well as the cosmics rate ($\sim 0.01\,\text{cm}^{-2}\,\text{sr}^{-1}\,\text{s}^{-1}$), the software is configured to select only X and Y coincidences (L0 trigger). On field, the trigger rate per channel ranges between 10 and 25 Hz. When the L1 trigger is applied (at the telescope level) this trigger rate decreases between 0.27 and 1.67 Hz.

When the photomultipliers of each telescope plane are calibrated, a dedicated cosmic run is started with the planes kept horizontal. The event selection is limited to the most vertical tracks which correspond to particles with a trajectory perpendicular to the planes of detection. The response of the telescope plane to the minimum ionising particles is measured using these vertical events and recorded for future offline data-correction.

The total cross-talk is then measured, it includes all possible sources: electronics, MAPM (coupling between anodes on the input window) and cookie-to-MAPM optical coupling. After alignment of the MAPM on the cookie 8 % of the total light signal sent on a pixel is shared by the neighbouring channels. Each MAPM pixel has 8 neighbours: 4 with a common side (each receiving about 2 % on the total light) and 4 at the corner which have a negligible role. For instance in the 16×16 matrices the clear fibres are connected only every two MAPM pixels so any confusion between cross-talk and multiple events is avoided. In field measurements, despite possible misalignments caused by the transportation vibrations, 3.25 % of the total light detected by a pixel is seen by its neighbours.

5.2 Acceptance of the telescope

The trajectory of a detected event is given by the X (i,k) and Y (j,l) coordinates of the two fired pixels belonging to the front ($P^{F}_{i,j}$) and rear ($P^{R}_{k,l}$) matrices of detection. All pairs of pixels, $\{P^{\mathrm{F}}_{i,j}, P^{\mathrm{R}}_{k,l}\}$ with the same relative position, $\{m = i - k, n = j - l\}$, share the same average direction, $\mathbf{r}_{m,n}$. The number of muons detected by the telescope for a given direction $\mathbf{r}_{m,n}$ reads,

$$N(\mathbf{r}_{m,n}, \Delta T) = I(\mathbf{r}_{m,n}) \times \Delta T \times \mathcal{T}(\mathbf{r}_{m,n}), \tag{2}$$

where I is the flux of muons given in $\mathrm{cm}^{-2}\,\mathrm{sr}^{-1}\,\mathrm{s}^{-1}$, ΔT is the duration of the measurement period, and $\mathcal{T}$ is the telescope acceptance expressed in $\mathrm{cm}^2\,\mathrm{sr}$. The acceptance may be written as,

$$\mathcal{T}(\mathbf{r}_{m,n}) = S(\mathbf{r}_{m,n}) \times \delta\Omega(\mathbf{r}_{m,n}), \tag{3}$$

where S is the detection surface and $\delta\Omega$ is the angular aperture. For a given direction $\mathbf{r}_{m,n}$, S is controlled by the pixel size d and by the number of pairs of pixels having a same $\{m,n\}$ and $\delta\Omega$ depends on the distance D between the matrices and on the distances x_{shift} and y_{shift} corresponding to m and n. Figure 13 shows the angular aperture and the acceptance for the $(2N_x - 1) \times (2N_y - 1) = 961$ discrete directions $\mathbf{r}_{m,n}$ of a telescope with two 16×16 matrices separated by $D = 115\,\mathrm{cm}$, as this shown in Fig. 10. As expected, the acceptance is maximal for the direction $\mathbf{r}_{0,0}$, perpendicular to the matrices, since all pixels contribute to the detection surface which is then maximum. The acceptance is small for a margin corresponding to the directions that most depart from $\mathbf{r}_{0,0}$ and only a fraction of all possible directions of detection will be efficient in practice. With $D = 115\,\mathrm{cm}$ and for the $\mathbf{r}_{0,0}$ direction, the solid angle is about $2 \times 10^{-3}\,\mathrm{sr}$, allowing to detect heterogeneities with a size of about 10 m at a distance of 500 m, in a few months. To reduce the detection time, two options increasing the solid angles can be considered: a reduction of the distance between the matrices or a merging of some angles of view in a post-processing to increase the solid angle of detection, both options affect the telescope resolution.

The actual acceptance of a telescope also depends on the efficiency of the scintillator bars forming the matrices. Depending on the quality of optical couplings, a scintillator bar may have a low response (see for example bar Y12 of the rear matrix, Fig. 14). This failure may be caused by a bad connection between optical fibres generated during transportation.

Having the number N of muons detected for each direction $\mathbf{r}_{m,n}$ during a period ΔT, the integrated flux I reads,

$$I(\mathbf{r}_{m,n}) = \frac{N(\mathbf{r}_{m,n})}{\Delta T \times \mathcal{T}(\mathbf{r}_{m,n})} \, (\mathrm{cm}^{-2}\,\mathrm{sr}^{-1}\,\mathrm{s}^{-1}). \tag{4}$$

The flux computed with the theoretical acceptance of the telescope (Fig. 13 middle) is shown on the top part of Fig. 15. As expected, this open sky flux varies principally with the zenith angle (Barrett et al., 1952) from $1 \times 10^{-4}\,\mathrm{cm}^{-2}\,\mathrm{sr}^{-1}\,\mathrm{s}^{-1}$ to $8.5 \times 10^{-3}\,\mathrm{cm}^{-2}\,\mathrm{sr}^{-1}\,\mathrm{s}^{-1}$, but one can observe several defects affecting the expected circular symmetry originated by the muon flux invariance with azimuth angles. These defects disappear if the acceptance model takes into account the Y12 bar failure, as shown in the right part of Fig. 13. The corrected muon flux recover its circular symmetry around the zenith as can be observed on the bottom part of Fig. 15. A more accurate calibration method of this sensor has been developed to correct any image distorsion due to more or less efficient bars, see Lesparre et al. (2011).

6 First field measurements

The installation of a muon telescope on field with harsh conditions requires first runs of calibration to ensure the sensor efficiency. We check the fluctuations with time of the total number of events detected and their distribution per bar to detect any loss in efficiency of the whole telescope or any bar failure (Fig. 14). The photomultipliers show the same gain and pedestal stabilities as in laboratory (Fig. 4). The cross-talk measured on field did not exhibit any changes despite vibrations during the transportation leading to possible changes in the cookie-MAPM alignment.

GID
1, 47–89, 2011

Four telescopes with $N_x = N_y = 16$ matrices are still operating in various field and weather conditions (Fig. 10): Mont-Terri underground laboratory, summit of Mount Etna in Sicily, Soufrière of Guadeloupe, Britanny in France (Marteau et al., 2011). We recorded consistent data sets to establish first radiographies of Mount Etna and Soufrière of Guadeloupe, besides series of measurement in the Mont Terri underground laboratory (Switzerland) will give us an access to establish a 3-D radiography with trajectories intersecting inside the solid rock.

The telescope installed on La Soufrière has now one year of measurement without any failure despite the hurricane season, strong wind occurrence and heavy rain episodes exceeding 100 mm day^{-1}. The monitoring of this telescope allows to check that the relative humidity inside the electronic containers varies around 70 % and that the dew point is far from being reached. Because of cloudy periods which may last a full week, the acquisition may be switched off because of power failure. A WiFi link allows the monitoring of the acquisitions interruption and relaunch. A three-planes detection configuration is used and only events in triple coincidence with a straight trajectory are retained. The presence of the third detection plane increases the purity of the data sample by filtering fake tracks, which may bias the analysis of the muon flux attenuation through matter (Nagamine, 2003). Analysis of current and past data samples is still underway while statistics is increasing and new actions are planned to better constrain our results (new open sky calibration runs in triple coincidence and completion of a Geant4 simulation model).

7 Conclusions and perspectives

In this article we detail the design, commissioning and running of scintillator telescopes dedicated to muon tomography of large geological structures such as volcanoes. The telescopes architecture is adapted from a well-known technology used in large high energy physics experiments such as OPERA.

GID
1, 47–89, 2011

Data acquisition are now underway on different field conditions while the data analysis is under development (Marteau et al., 2011). A calibration method to correct bars different efficiencies has been established (Lesparre et al., 2011). The telescope commissioning and running protocols are validated.

We prospect the MPPC option to replace the MAPMs. Tests and comparisons are underway to produce quickly a new hybrid telescope mixing both photosensors. As the telescope set up is confirmed, bigger matrices with 24×32 pixels are in construction to improve the telescope acceptance. Each telescope developed for an installation in open sky will be equipped with three matrices at least in order to increase the signal to noise ratio and therefore the images contrast. After the completion of the exploratory steps detailed in the present article a very rich and promising programme of data taking, research and development as well as modelization are now established.

Acknowledgements. The design and the construction of the telescopes greatly benefited from the skilled expertise of Karim Mahiouz, Franck Mounier and Pascal Rolland (mechanical engineering) and Sylvain Vanzetto (optical fibres). Optical plugs are designed and machined by Troimeca, and the tarpaulins are manufactured by Tigier. Daniele Carbone, Sylvain Pasquet and Justine Restout participated to the construction of the telescopes. The field installation on La Soufrière de Guadeloupe benefited from the generous help of the Observatoire Volcanologique et Sismologique de Guadeloupe staff, particularly from: Jean-Bernard De Chabalier, Alexis Bosson, Frédéric Randriamora, Thierry Kitou, Christian Lambert and Véronique Daniel. The DIAPHANE project is financially supported by the IPGP (www.ipgp.fr) BQR grant, the DOMOSCAN ANR project (http://www.agence-nationale-recherche.fr), the CNRS/IN2P3 (www.cnrs.fr) Astroparticles program, and the MD experiment of the Mont Terri project (http://www.mont-terri.ch) funded by Swisstopo and CRIEPI partners. This is IPGP contribution 3247.

GID

1, 47–89, 2011

A field telescope for cosmic ray geophysical tomography

N. Lesparre et al.

References

Adam, T., Baussan, E., Borer, K., Campagne, J. E., Chon-Sen, N., De La Taille, C., Dick, N., Dracos, M., Gaudiot, G., Goeltzenlichter, T., Gornushkin, Y., Grapton, J.-N., Guyonnet, J-L., Hess, M., Igersheim, R., Janicsko Csathy, J., Jollet, C. Juget, F., Kocher, H., Krasnoperov, A., Krumstein, Z., Martin-Chassard, G., Moser, U., Nozdrin, A., Olchevski, A., Porokhovoi, S., Raux, L., Sadovski, A., Schuler, J., Schütz, H.-U., Schwab, C., Smolnikov, A., Van Beek, G., Vilain, P., Wälchli, T., Wilquet, G., and Wurtz, J.: The OPERA experiment target tracker, Nucl. Instrum. Meth. A, 577, 523–539, doi:10.1016/j.nima.2007.04.147, 2007. 52

Alvarez, L. W., Anderson, J. A., Bedwei, F. E., Burkhard, J., Fakhry, A., Girgis, A., Goneid, A., Hassan, F., Iverson, D., and Lynch, G.: Search for hidden chambers in the pyramids, Science, 167, 832–839, 1970. 48

Barrett, P., Bollinger, L. M., Cocconi, G., Eisenberg, Y., and Greisen, K.: Interpretation of cosmic-ray measurements far underground, Rev. Mod. Phys., 24, 133–178, 1952. 48, 65

Bellamy, E. H., Bellettini, G., Budagov, J., Cervelli, F., Chirikov-Zorin, I., Incagli, M., Lucchesi, D., Pagliarone, C., Tokar, S., and Zetti, F.: Absolute calibration and monitoring of a spectrometric channel using a photomultiplier, Nucl. Instrum. Meth. A, 339, 468–476, doi:10.1016/0168-9002(94)90183-X, 1994. 61, 62

Bouchel, M., Callier, S., Dulucq, F., Fleury, J., De La Taille, C., Martin-Chassard, G., and Raux L.: SPIROC (SiPM Integrated Read-Out Chip): dedicated very front-end electronics for an ILC prototype hadronic calorimeter with SiPM read-out, in: Proceedings of Topical Workshop on Electronics for Particle Physics, Paris, France, 21–25 September 2009, 504–508, 2009. 56

De Asmundis, R., Avella, P., and Toglia, F.: Using RPC detectors as cosmic rays monitor, IEEE T. Nucl. Sci., 54, 670–676, doi:10.1109/TNS.2007.895505, 2007. 50

Gaisser, T. K. and Stanev, T.: Cosmic rays, in: Review of particle properties, edited by: Alvarez-Gaumé, L., Blaizot, J. P., Cvetic, M., Doser, M., Geesaman, D. F., Giudice, G. F., Grinstein, B., Haxton, W., Metag, V., Ringwald, A., Rolandi, L., Schlatter, W. D., Weerts, H., and Yanagida, T., Phys. Rev. Lett., 667, 254–260, doi:10.1016/j.physletb.2008.07.028, 2008. 48

Gibert, D., Beauducel, F., Déclais, Y., Lesparre, N., Marteau, J., Nicollin, F., and Tarantola, A.: Muon tomography: plans for observations in the lesser antilles, Earth Planets Space, 62, 153–165, doi:10.5047/eps.2009.07.003, 2010. 50

Giomataris, I., De Oliveira, R., Andriamonje, S., Aune, S., Charpak, G., Colas, P., Fanourakis,

G., Ferrer, E., Giganon, A., Rebourgeard, P., and Salin, P.: Micromegas in a bulk, Nucl. Instrum. Meth. A, 560, 405–408, doi:10.1016/j.nima.2005.12.222, 2006. 50
Girerd, C., Gardien, S., Burch, J., Katsanevas, S., and Marteau, J.: Ethernet network-based DAQ and smart sensors for the OPERA long-baseline neutrino experiment, in: IEEE Nucl. Sci. Conf. R., Lyon, France, 15–20 October 2000, 2, 12/111–12/115, doi:10.1109/NSSMIC.2000.949950, 2000. 55
Hebbeker, T. and Timmermans, C.: A compilation of high energy atmospheric muon data at sea level, Astropart. Phys., 18, 107–127, doi:10.1016/S0927-6505(01)00180-3, 2002.
Lesparre, N., Gibert, D., Marteau, J., Déclais, Y., Carbone, D., and Galichet, E.: Geophysical muon imaging: feasibility and limits, Geophys. J. Int., 183, 1348–1361, doi:10.1111/j.1365-246X.2010.04790.x, 2010. 49, 51
Lesparre, N., Gibert, D., and Marteau, J.: Bayesian dual inversion of experimental telescope acceptance and integrated flux for geophysical muon tomography, Geophys. J. Int., doi:10.1111/j.1365-246X.2011.05268.x, in press, 2011. 49, 65, 67
Longland, R., Iliadis, C., Champagne, A. E., Fox, C., and Newton, J. R.: Nuclear astrophysics studies at the LENA facility: The γ-ray detection system, Nucl. Instrum. Meth. A, 566, 452–464, doi:10.1016/j.nima.2006.07.006, 2006.
Lucotte, A., Bondil, S., Borer, K., Campagne, J. E., Cazes, A., Hess, M., De La Taille, C., Martin-Chassard, G., Raux, L., and Repellin, J. P.: A front-end read out chip for the OPERA scintillator tracker, Nucl. Instrum. Meth. A, 521, 378–392, doi:10.1016/j.nima.2003.10.104, 2004. 54
Malmqvist, L., Jonsson, G., Kristiansson, K., and Jacobsson, L.: Theoretical studies of in-situ rock density determination using cosmic-ray muon intensity measurements with application in mining geophysics, Geophysics, 44, 1549, doi:10.1190/1.1441026, 1979. 48
Marteau, J.: The OPERA global readout and GPS distribution system, Nucl. Instrum. Meth. A, 617, 291–293, doi:10.1016/j.nima.2009.10.095, 2010. 55, 57
Marteau, J., Gibert, D., Lesparre, N., Nicollin, F., Noli, P., and Giacoppo, F.: Muons tomography applied to geosciences and volcanology, Nucl. Instrum. Meth. A, doi:10.1016/j.nima.2011.11.061, in press, 2011. 50, 66, 67
MINERvA collaboration: The MINERvA technical design report, 2006. 51
Mohammad-Djafari, A. and Dinten, J. M.: Tomographic reconstruction from few projections, in: Bayesian approach to inverse problems, digital signal and image processing series, edited by: Idier, J., ISTE Ltd and John Wiley & Sons In, London, United Kingdom, 307–334, 2008.

49
Nagamine, K.: Geo-tomographic observation of inner-structure of volcano with cosmic-ray muons, J. Geogr., 104, 998–1007, 1995. 48
Nagamine, K.: Introductory to muon science, Cambridge university press, New York, United States of America, 2003. 48, 59, 66
Nagamine, K., Iwasaki, M., Shimomura, K., and Ishida K.: Method of probing inner-structure of geophysical substance with the horizontal cosmic-ray muons and possible application to volcanic eruption prediction, Nucl. Instrum. Meth. A, 356, 585–595, doi:10.1016/0168-9002(94)01169-9, 1995. 48
OPERA collaboration: A long baseline ν_τ appearance experiment in the CNGS beam from CERN to Gran Sasso, Progress Report, 1999. 51
Pla-Dalmau, A., Bross, A. D., and Mellott, K. L.: Low-cost extruded plastic scintillator, Nucl. Instrum. Meth. A, 466, 482–491, doi:10.1016/S0168-9002(01)00177-2, 2001. 50, 51
Pla-Dalmau, A., Bross, A. D., and Rykalin, V. V.: Extruding plastic scintillator at Fermilab, in: IEEE Nucl. Sci. Conf. R., Portland, Oregon United States of America, 19–25 October 2003, 1, 102–104, doi:10.1109/NSSMIC.2003.1352007, 2003. 51
Pla-Dalmau, A., Bross, A. D., Rykalin, V. V., and Wood, B. M.: Extruded plastic scintillator for MINERvA, in: IEEE Nucl. Sci. Conf. R., Wyndham El Conquistador Resort, Puerto Rico, 23–29 October 2005, 1, 1298–1300, doi:10.1109/NSSMIC.2005.1596558, 2005. 51
Tanaka, H. K. M., Nagamine, K., Kawamura, N., Nakamura, S. N., Ishida, K., and Shimomura, K.: Development of a two-fold segmented detection system for near horizontally cosmic-ray muons to probe the internal structure of a volcano, Nucl. Instr. Meth. A, 507, 657–669, doi:10.1016/S0168-9002(03)01372-X, 2003. 48
Tanaka, H. K. M., Nagamine, K., Nakamura, S. N., and Ishida, K.: Radiographic measurements of the internal structure of Mt. West Iwate with near-horizontal cosmic-ray muons and future developments, Nucl. Instrum. Meth. A, 555, 164–172, doi:0.1016/j.nima.2005.08.099, 2005. 49, 50
Tanaka, H. K. M., Nakano, T., Takahashi, S., Yoshida, J., and Niwa, K.: Development of an emulsion imaging system for cosmic-ray muon radiography to explore the internal structure of a volcano, Mt. Asama, Nucl. Instrum. Meth. A, 575, 489–497, doi:10.1016/j.nima.2007.02.104, 2007. 50
Tanaka, H. K. M., Uchida, T., Tanaka, M., Takeo, M., Oikawa, J., Ohminato, T., Aoki, Y., Koyama, E., and Tsuji, H.: Detecting a mass change inside a volcano by cosmic-ray muon radiography

GID
1, 47–89, 2011
A field telescope for cosmic ray geophysical tomography
N. Lesparre et al.

(muography): First results from measurements at Asama volcano, Japan, Geophys. Res. Lett., 36, L17302, doi:10.1029/2009GL039448, 2009. 49

Tanaka, H. K. M., Taira, H., Uchida, T., Tanaka, M.,Takeo, M., Ohminato, T., Aoki, Y., Nishitama, R., Shoji, D., and Tsuiji, H.: Three-dimensional computational axial tomography scan of a volcano with cosmic ray muon radiography, J. Geophys. Res., 115, B12332, doi:10.1029/2010JB007677, 2010. 49

GID

1, 47–89, 2011

Table 1. Characteristics of the Hamamatsu's H8804 MAPM and S10362-11 MPPC.

Hamamatsu H8804 MAPM
Photocathode material: bialkali Window material: borosilicate Spectral response: 300–650 nm Wavelength of maximum response: 420 nm Typical quantum efficiency: 16 % Number of dynode stages: 12 Anode size: $2 \times 2\,mm^2$ Maximum supply voltage between anode and cathode: 1000 V Gain at 800 V: 3.0×10^5 Cross talk (with 1 mm optical fibre): 2 % Uniformity among all anodes: 1 : 3
Hamamatsu S10362-11 MPPC
Spectral response: 320–900 nm Wavelength of maximum response: 440 nm Photon detection efficiency: 50 % (including cross-talk and after pulses) Number of pixels: 400 Pixel size: $50 \times 50\,\mu m^2$ Effective active area: $1 \times 1\,mm^2$ Operating voltage: 70 ± 10 V Gain at nominal voltage: 7.5×10^5 Dark count: 400 kcps

GID
1, 47–89, 2011

GID
1, 47–89, 2011

Table 2. On-board computer characteristics.

CPU	VIA Esther 1,2 GHz/RAM 1 Go
Storage	SSD 64 Go (low consumption, robustness)
Ports	2 Ethernet, 2 USB and 1 RS232
Cooling mode	Passive
Consumption	13 W
Tension	5 V
Size	170/124/38 mm

Table 3. Electrical consumption of the devices.

Component	Consumption W
Acquisition boards	2×7
WiFi antenna	3
On-board computer	13
Ethernet switch	2.5
DC/DC converters	3
Data logger (in wake-up mode)	0.1
Total	≈ 36

GID
1, 47–89, 2011

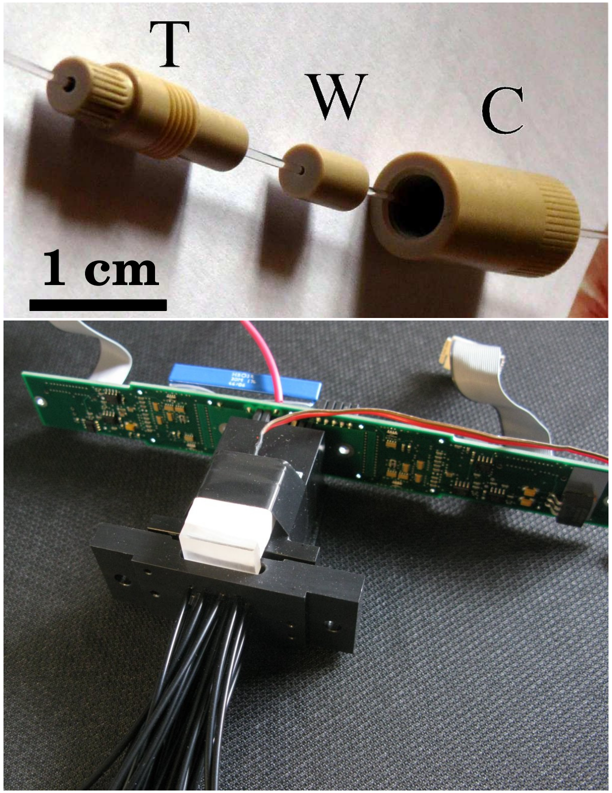

Fig. 1. Top: the three parts of an optical plug: part (T) receives the WLS fibre and its grooved end is inserted and glued in the scintillator bar. The clear fibre is glued in the small "whiz-bang" (W), and the cap (C) is screwed on part (T) to maintain the polished ends of the WLS and clear fibres face to face. Bottom: view of the clear fibres glued in the cookie fixed in front of the MAPM window. The transparent acrylic piece fixed on the cookie contains a LED used to calibrate the MAPM channels. The front end board is also visible.

GID
1, 47–89, 2011

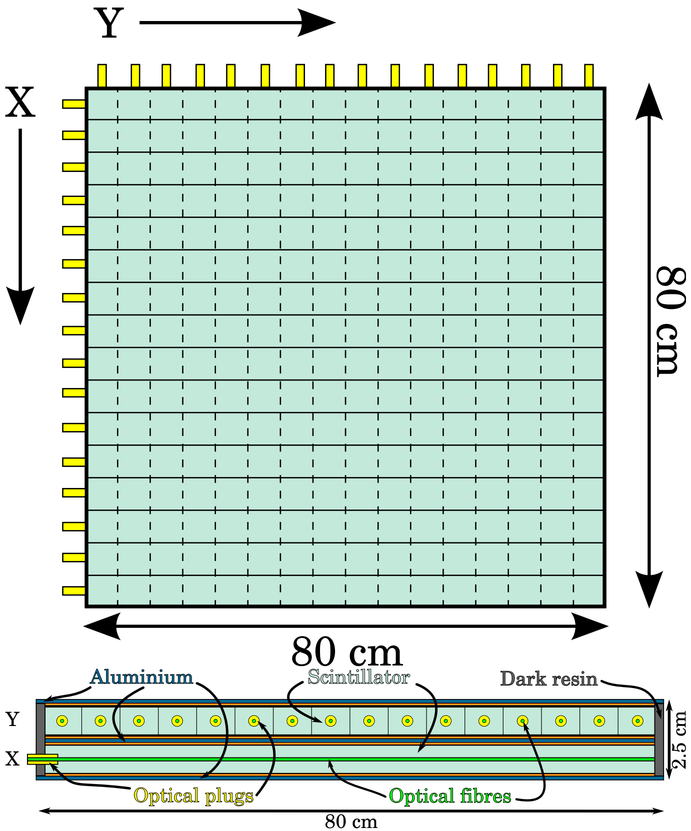

Fig. 2. Top: schematic view of a matrix with 16 × 16 pixels, an area of $0.8 \times 0.8 = 0.64\,m^2$ and one optical plug at one extremity of each bar. Bottom: cross-section view.

GID
1, 47–89, 2011

A field telescope for cosmic ray geophysical tomography

N. Lesparre et al.

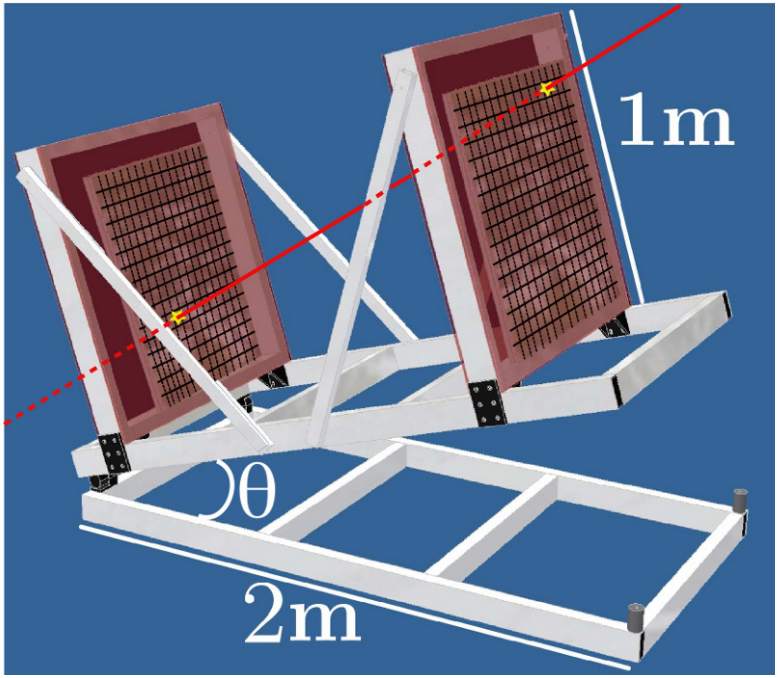

Fig. 3. Schematic view of a muon telescope equipped with two matrices with 16 × 16 pixels.

GID
1, 47–89, 2011

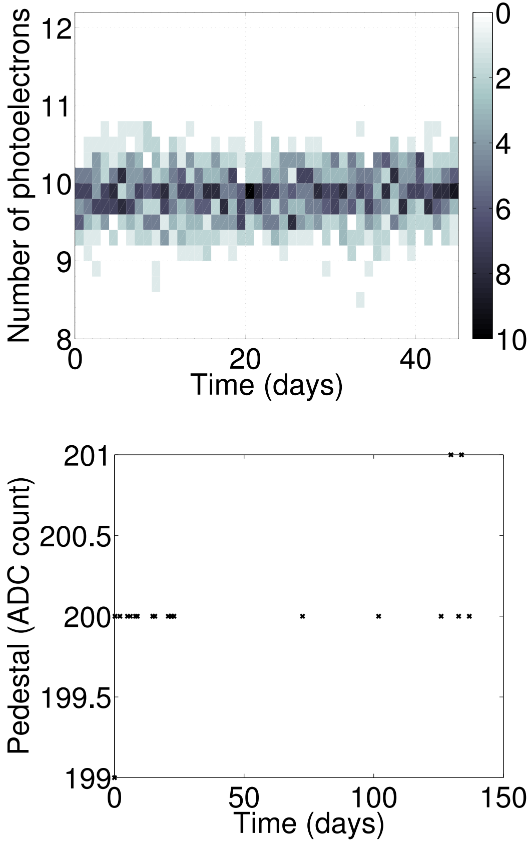

Fig. 4. MAPM stability with time on field. Top: distribution of one MAPM channel gain with time. The gain is expressed in units of photo-electrons recorded for a crossing minimum ionising particle. Bottom: variation of the MAPM pedestals with time.

GID
1, 47–89, 2011

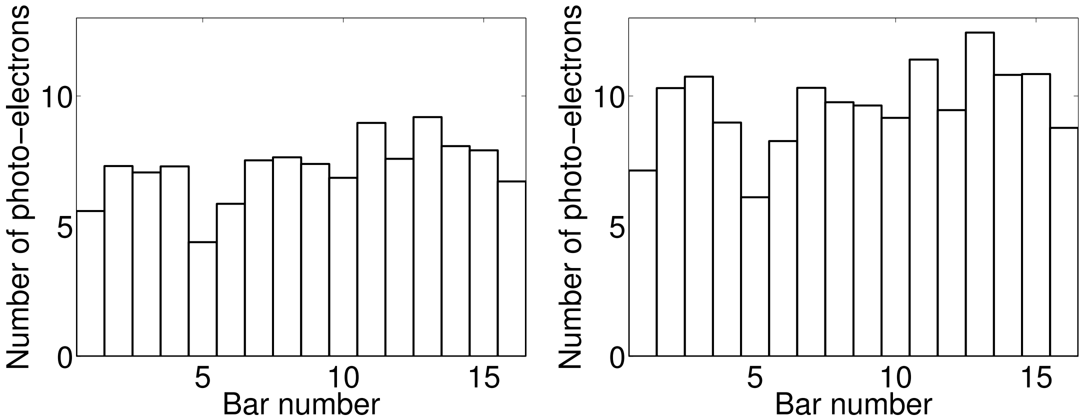

Fig. 5. Light yield comparison for a telescope plane readout with a standard MAPM (mod5, left) and an "extended photocathode" MAPM (200-mod5, right), expressed in number of photo-electrons recorded for a crossing minimum ionising particle.

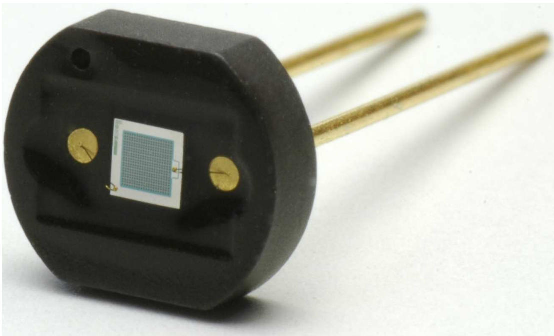

Fig. 6. Picture of a ceramic packaged MPPC (picture from Hamamatsu).

GID
1, 47–89, 2011

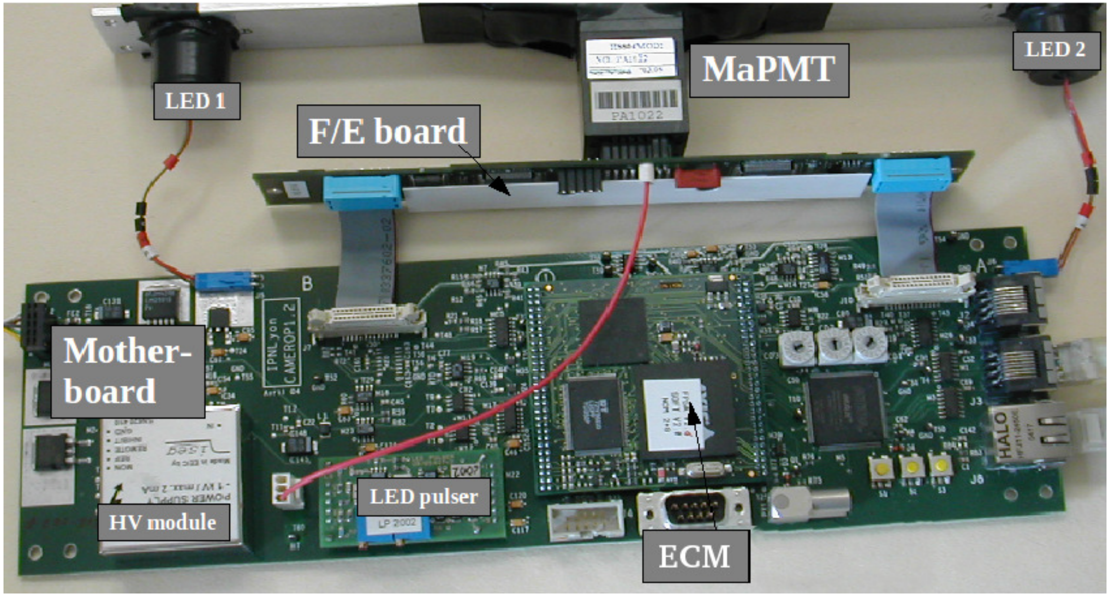

Fig. 7. Readout system for MAPM. The front-end board, connecting the MAPM, has two multichannel chips for the trigger generation and the signal readout. The mother-board hosts the Ethernet Controller Module, the High Voltage module, the LED pulser system and the clock readout devices.

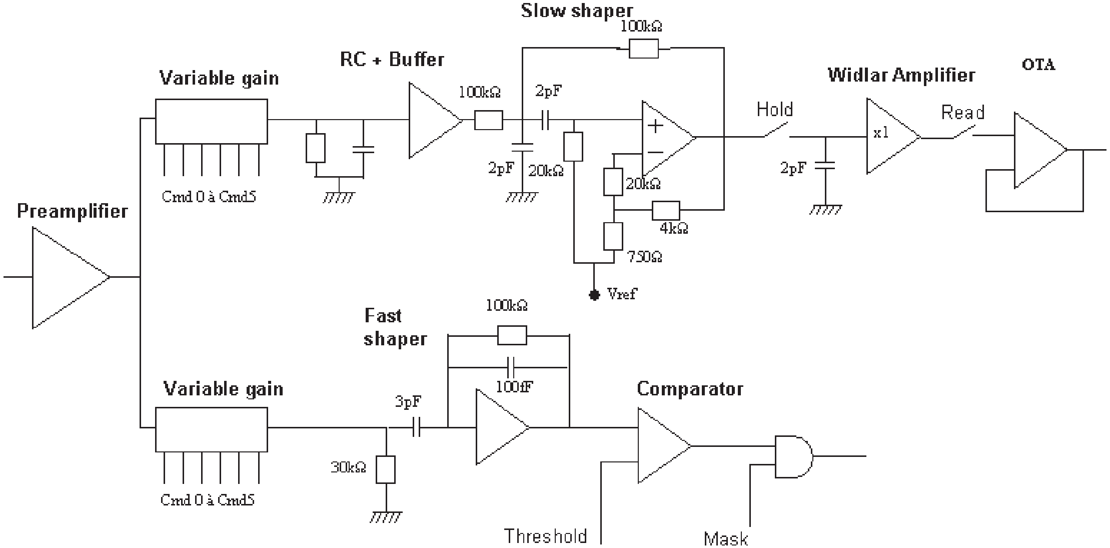

Fig. 8. Architecture of one channel of a front-end chip.

GID
1, 47–89, 2011

A field telescope for cosmic ray geophysical tomography

N. Lesparre et al.

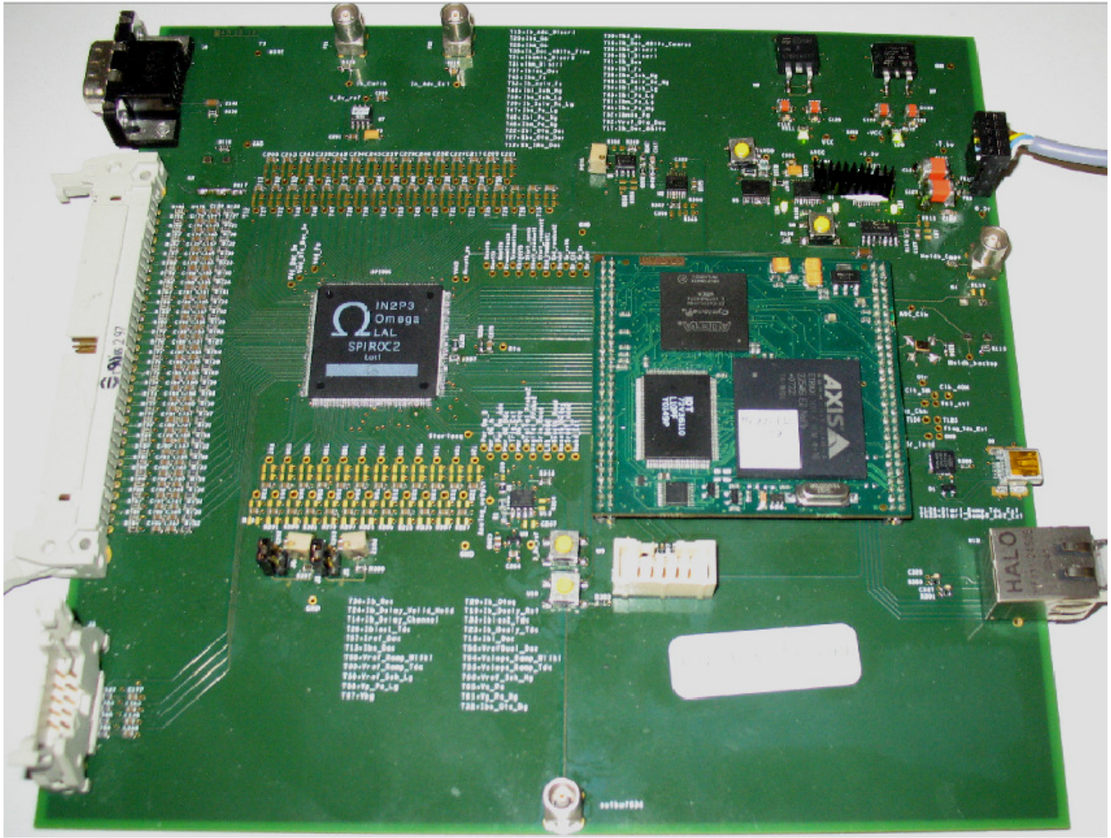

Fig. 9. Picture of the complete readout board for the MPPC option.

GID

1, 47–89, 2011

A field telescope for cosmic ray geophysical tomography

N. Lesparre et al.

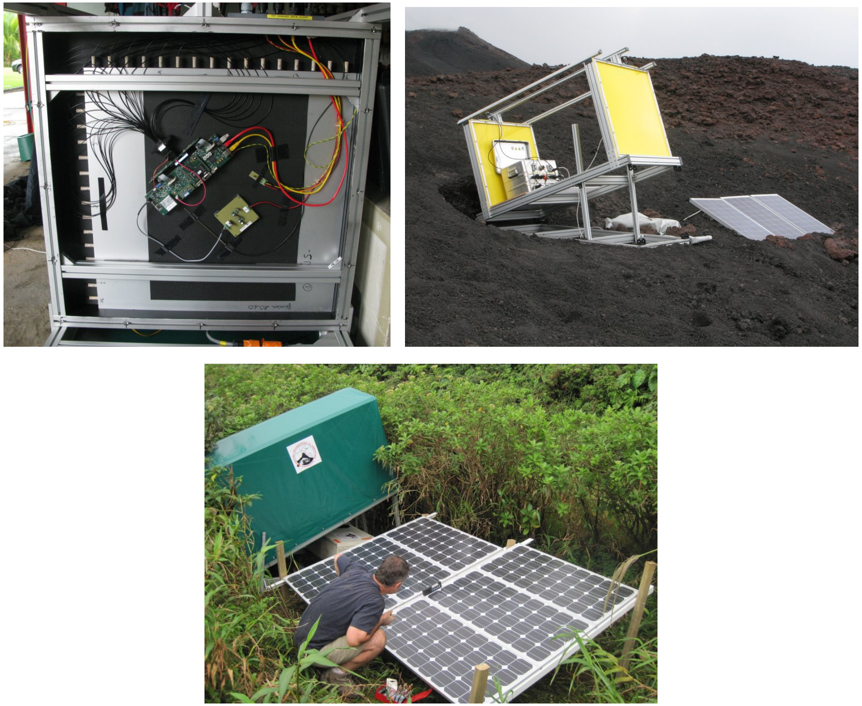

Fig. 10. Left: matrix with open case. Middle: complete telescope at the summit of Mount Etna in Sicily. The dip is 30° and the distance between the two matrices is of 115 cm. Solar conditions there allow single solar unit use. Right: telescope covered with its tarpaulin on La Soufrière of Guadeloupe. Two solar units of 270 W each are mandatory because of cloudy weather.

GID
1, 47–89, 2011

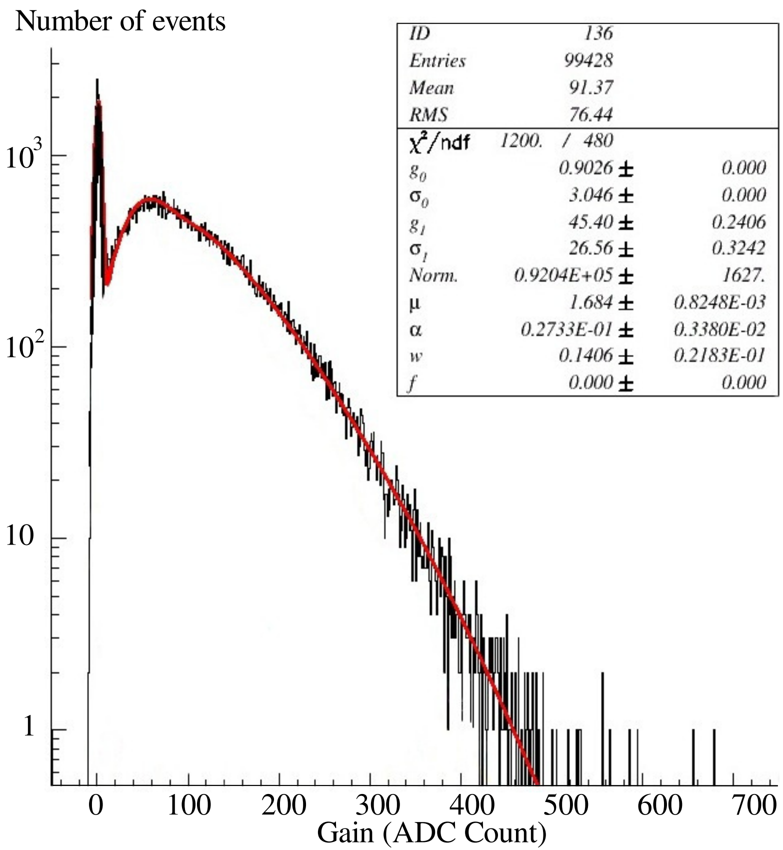

Fig. 11. Typical gain distribution on a particular channel. The red curve represents the response signal $\mathcal{R}_{\text{MAPM}}$ to a light pulse whose parameters are defined in the text.

GID
1, 47–89, 2011

A field telescope for cosmic ray geophysical tomography

N. Lesparre et al.

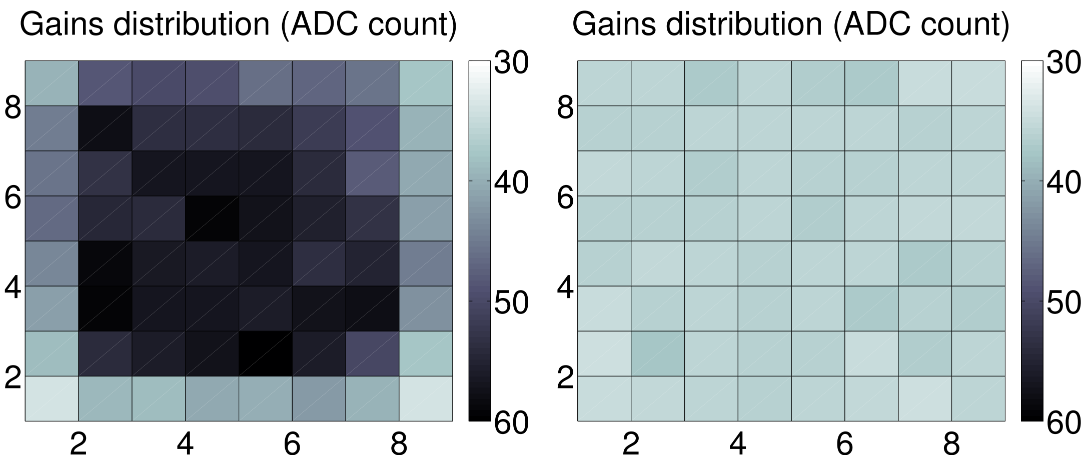

Fig. 12. Gains distribution over the 8 × 8 matrix before (left) and after (right) gain correction.

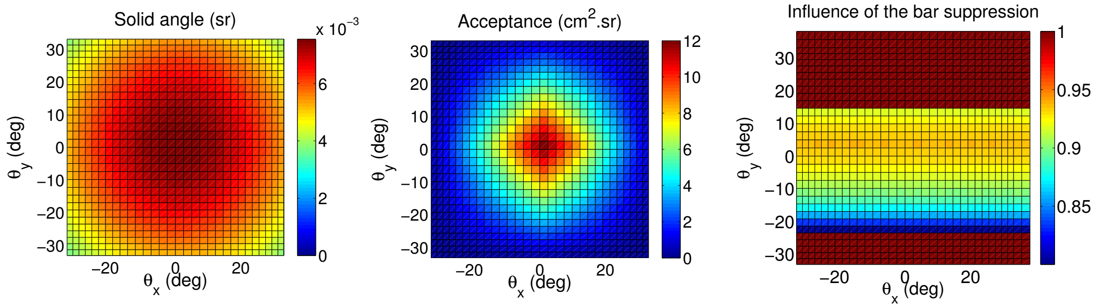

Fig. 13. Azimuthal angular properties of a telescope equipped with two 16×16 matrices with pixel size $d = 5$ cm and separated by $D = 115$ cm. Left: angular resolution $\delta\Omega$ for each discrete direction $\mathbf{r}_{m,n}$. Middle: acceptance $\mathcal{T}(\mathbf{r}_{m,n})$. Right: ratio of the corrected acceptance taking into account for the dysfunction of the bar Y12 of the rear matrix on the theoretical acceptance computed with all bars (Fig. 14).

GID
1, 47–89, 2011

A field telescope for cosmic ray geophysical tomography

N. Lesparre et al.

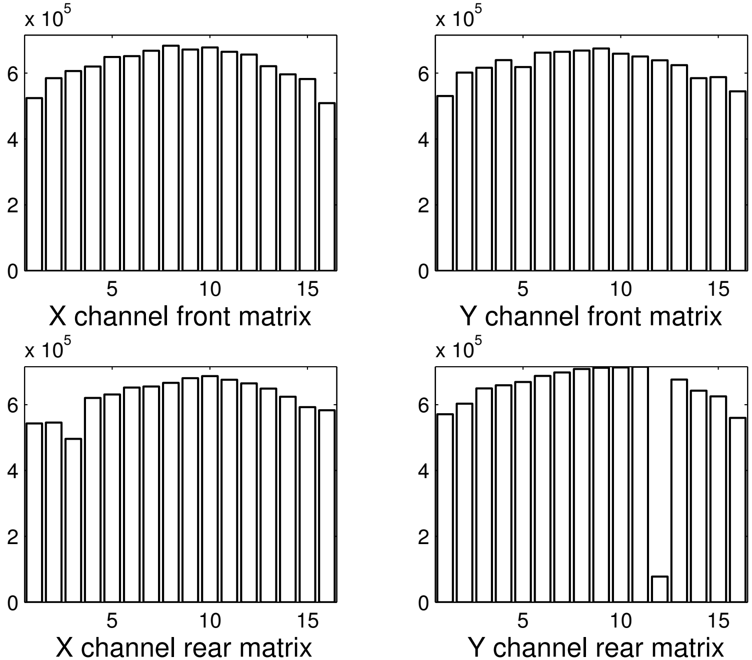

Fig. 14. Events distribution detected on the front and rear X and Y planes. The data are collected during 170 h under a zenith angle of 1.35° and for an azimuth angle of 45°.

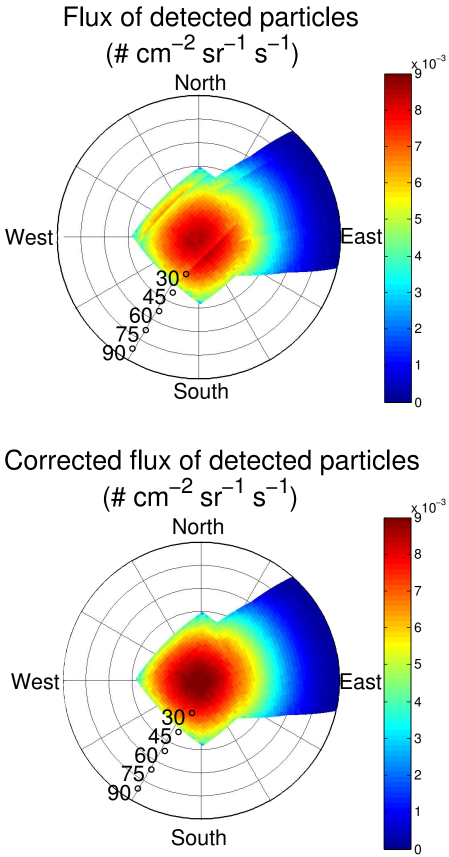

Fig. 15. Top: detected flux in open sky conditions. Number of particles detected divided by the acquisition time and the theoretical telescope acceptance. Bottom: corrected flux of particles detected, computed with the acceptance on right Fig. 13. The zenith angles are indicated.

GID
1, 47–89, 2011

A field telescope for cosmic ray geophysical tomography

N. Lesparre et al.